Operando Visualization of Water Distribution in Gas Diffusion Media of PEFCs with an Optimized Neutron Grating Interferometer

M. Siegwart,[1,2] V. Manzi-Orezzoli,[1] J. Valsecchi,[2] R. P. Harti,[2] M. Kagias,[3] M. Strobl,[2] C. Grünzweig,[2] T. J. Schmidt,[1,4,*] and P. Boillat[1,2,**,z]

[1]*Electrochemistry Laboratory (LEC), Paul Scherrer Institut (PSI), 5232 Villigen PSI, Switzerland*
[2]*Laboratory for Neutron Scattering and Imaging (LNS), Paul Scherrer Institut (PSI), 5232 Villigen PSI, Switzerland*
[3]*Swiss Light Source (SLS), Paul Scherrer Institut (PSI), 5232 Villigen PSI, Switzerland*
[4]*Laboratory of Physical Chemistry, ETH Zürich, 8093 Zürich, Switzerland*

We demonstrated the use of a neutron grating interferometer setup (nGI) with a significantly improved contrast-to-noise ratio of the operando dark-field (DF) contrast visualization of water in gas diffusion media (GDM). The nGI parameters were optimized in such a way that we could perform DF imaging of a fully operational fuel cell including two GDM layers (anode and cathode side). The DF contrast is sensitive to the size and shape of microstructures and is in principle not influenced by large water clusters present in flow field channels. Thus, DF imaging can be applied to analyze water present in GDM overlapping with channels, which is not possible by attenuation contrast imaging when the cell is placed perpendicular to the beam direction. In GDM regions overlapping with ribs the distinction of hydrophilic and hydrophobic areas is facilitated as well compared to attenuation contrast imaging. Finally, we show that disturbing artefacts introduced by moving water clusters in the channels are considerably reduced by applying a *golden ratio* phase stepping scan strategy.

Polymer electrolyte fuel cells (PEFCs) convert the chemical energy stored in hydrogen into electrical energy without the emission of carbon dioxide or pollutants. Thus, they are promising candidates to play a crucial role in the future hydrogen economy for powering mobile (i.e. cars) or stationary (i.e. back-up power) applications. Hydrogen is oxidized at the anode and the protons are conducted through the polymer electrolyte membrane to the cathode catalyst layer, where they combine with oxygen to form water. The product water of the electrochemical reaction either diffuses as a gas or flows as a liquid through the porous gas diffusion media (GDM) to the gas flow channels. The GDM plays a crucial role for a well-balanced water management. The membrane has to be hydrated to be proton conductive, but liquid water accumulations in the pores of the GDM hinder the access of gases to the catalyst layer, which leads to mass transport losses, especially at high power densities.[1–6] A well-balanced water management is also crucial to avoid degradation and ensure a long PEFC life-time.[7] GDM usually consist of two separate layers, the gas diffusion layer (GDL) and the microporous layer (MPL). Both the GDL and MPL properties vary for different manufacturers and various types are available, but for most applications the GDL is made of carbon fibers with a diameter of about 7–10 μm.[8] The thickness of the GDL varies between 110 and 440 μm[9–12] with a porosity usually around 70%–80%.[9,11–14] The pore size distribution is broad and usually covers a range between ~1–100 μm[5,10,11,15] and the mean pore diameter for a GDL of the type Freudenberg H2315 was measured to amount to 16.5 μm.[15] It is usual to coat the GDL fibers with fluoropolymers (e.g polytetrafluoroethylene) to avoid accumulation of water[16,17] in the GDL. The MPL is commonly made of carbon and fluoropolymer particles and is normally located between the GDL and catalyst layer. It has pores in the range of approximately 0.01 μm to 1 μm.[18] As reviewed by Park et al.[19] and Lapicque,[20] GDM can suffer from degradation under harsh conditions such as cold starts, freeze-thaw cycles,[21] by

repeated compression cycles due to temperature or humidity variations[22] or due to the steady compression force applied onto GDM mounted inside a PEFC stack. This can result, for example, in a change of the microstructure,[22] fiber breaking[23] or in the loss of hydrophobic coating.[21]

Various characterization techniques have been applied to correlate GDM properties with the water distribution within the GDM and the PEFC performance as summarized in brief below and reviewed in details by Bazylak[24] and Arvay et al.[25] Similar characterization techniques are frequently used to investigate the GDM integrity during operando or post mortem experiments. Attenuation contrast X-ray radiography and tomography are—thanks to the high spatial and temporal resolution, in particular when using a synchrotron beam—powerful tools to analyze GDM microstructure[11,26] or water in pores of the GDM during operando experiments under stationary and/or transient operation conditions.[2,27–33] However, the cell size for such experiments is limited to small active areas due to the low transparency of the cell materials. Moreover, for measurements with a synchrotron beam, damage to the fuel cell is a concern.[34,35] Other imaging methods such as optical imaging using partially transparent flow fields and a CCD camera,[36–38] imaging with an environmental scanning electron microscope (ESEM)[39] in combination with freezing (cryo-SEM)[40] or magnetic resonance imaging[41,42] are occasionally used to analyze the water distribution within fuel cell components. However, one of the most widely applied methods for operando analysis is neutron imaging. Neutrons are transmitted well through fuel cell materials (such as aluminum, steel and graphite) and provide a high contrast for water in attenuation contrast images. Therefore, various researchers used neutron attenuation contrast imaging to study, for example, the influence of the material of fuel cell components,[17,43,44] flow field designs,[45–48] compression ratio of the GDM[49] and operation conditions[50–53] on the water distribution and performance. An extensive review about neutron imaging to study fuel cells was reported by Boillat et al.[54] To study the water distribution within the plane of the cell, the membrane electrode assembly (MEA) is placed perpendicular to the beam. In this configuration one cannot distinguish between water in GDM and channels or water present in anode and cathode channels unless

special purging procedures are applied[55,56] or different flow field geometries are used at the anode and cathode.[57] To distinguish water present in different layers of the cell (i.e. channels and GDM), the MEA is usually placed parallel to the beam axis.[4,17,44,48,58,59]

Using X-ray or neutron attenuation contrast imaging it was found, for example, that water content in the GDM is higher under the ribs than under the channels.[4,28,30,58,59] Other valuable insights were obtained about the influence of the MPL on improved water management[27,29,31,33,58] or about the relation between hydrophobic coating of GDL fibers, water content in the GDL and mass transport losses.[17] Such findings helped to boost fuel cell performance by improving water management through improvements of GDM properties. The fabrication of GDM with hydrophilic pathways,[44] which improve water removal under the ribs, is one out of many examples for this.

However, the cell dimension in beam direction is limited for neutron imaging when the MEA is placed parallel to the beam axis to less than 20 mm (assuming that 50% of GDM pores are water filled), because a water thickness of 10 mm in beam direction leads to saturation of the transmission signal for the spectrum of common imaging beam lines. Therefore, the analysis of water distributed in the GDM of large cells is challenging with currently available characterization techniques and methods beyond simple attenuation contrast imaging are required. Following our first publication about the possibility of using *neutron dark field imaging* to specifically visualize water in the gas diffusion layers,[60] we present here respective capabilities and application of the method but also some identified limitations for operando analysis.

Neutron dark-field (DF) imaging is a technique which is not yet commonly applied for the characterization of fuel cells, whereas it bears a high potential to provide information about the water distribution in GDM and GDM damages during operando experiments. DF contrast is generated when neutrons are scattered by microstructures to ultra-small angles and DF imaging allows measuring this scattering signal with spatial resolution. DF imaging is performed with grating interferometers (GI) designed for neutrons (nGI)[61] or X-rays (xGI)[62] and is an established technique for analyzing the microstructure for various samples.[63–69] Large structures (>few hundred μm) do not scatter neutrons to the angles to which the setup is sensitive and thus do not influence the DF value. Therefore, DF imaging can be applied to selectively visualize water in the pores of GDM without the disturbing signal of water accumulations in channels. Previously, we confirmed that the DF value changes significantly when a dry GDL mounted in an ex situ test rig is filled with heavy water.[60] Moreover, we demonstrated that DF imaging can be applied to identify damaged GDL areas. Here, we report about an optimized nGI setup for the analysis of water distributed in the pores of GDM during fuel cell operation. Further, we corroborate that microstructural inhomogeneities in GDM can be visualized during operando experiments using DF imaging. Thanks to the improved nGI setup, we obtained DF images with a significantly improved contrast-to-noise ratio compared to previously presented implementations.[61,70,71] This improves applicability of DF imaging considerably and allows higher sensitivity to small variations in the DF contrast and/or measurements with higher temporal and/or spatial resolution.

Theoretical Background

In most cases, an nGI consists of three gratings (one phase grating and two absorption gratings).[61] The source grating (G0) is used to fulfill the spatial coherence requirement of the interferometer. The phase grating (G1) produces an interference pattern at given distances (Talbot distances), which is detected with the help of the analyzer grating (G2). The interference pattern measured without sample (open beam) is characterized by its *visibility* (V_0) (fringe contrast), which is the ratio of its modulation amplitude divided by the mean value of the beam intensity:

$$V_0 = \frac{I_{\max} - I_{\min}}{I_{\max} + I_{\min}} \qquad [1]$$

Scattering of neutrons (e.g. by microstructures) to ultra-small angles redistributes intensities between modulation maxima and minima and thus reduces the visibility.[72] Acquiring images with one of the gratings in different positions (using phase-stepping[61,73,74]) allows quantifying the loss of visibility in every pixel of the imaging detector. Thus, the impact of scattering is measured with spatial resolution. The DF value is related to the visibility described by Eq. 1 and can be determined as:

$$DF - value = \frac{V_S}{V_0} = e^{t\Sigma_S(G(\xi_{GI})-1)}, \qquad [2]$$

where V_S and V_0 are the measured visibilities with and without the sample, respectively, t is the thickness of the sample, $\sum_S$ the total macroscopic scattering cross section and $G(\xi_{GI})$ is the projected real space correlation function,[63,75,76] with depends on the autocorrelation length of the sample determined by intra- and inter-particle correlations (e.g. size, form, ordering) and the autocorrelation length of the GI setup ξ_{GI}. As derived in Ref. 72, ξ_{GI} is given by:

$$\xi_{GI} = \frac{\lambda L_S}{p_2}, \qquad [3]$$

where λ is the neutron wavelength, L_S is the distance between sample and G2 (when the sample is placed downstream of G1) and p_2 is the period of G2. The macroscopic scattering cross section $\sum_S$ is described, for a two-phase sample, by the following equation[75]:

$$\sum_s = \lambda^2 (\Delta SLD)^2 \phi_v (1 - \phi_v) \alpha, \qquad [4]$$

where ΔSLD is the difference of the scattering length density (SLD) between the two considered materials, ϕ_v the volume fraction of one phase and α is a parameter describing the effective average structure size.

In two phase systems, the projected real space correlation function $G(\xi_{GI})$ can be considered as being the probability that two randomly chosen points with the distance ξ_{GI} between them are within the same phase. Therefore, the function $1 - G(\xi_{GI})$ can be considered as the probability that two randomly chosen points with the distance ξ_{GI} between them are in two different phases. When ξ_{GI} is significantly smaller than the size of the structures in the material, the probability that the path between two points separated by a distance ξ_{GI} crosses two interfaces is negligible. Therefore, in this case, $1 - G(\xi_{GI})$ is proportional to the probability of having one interface between these two points, i.e. to the surface area. As illustrated in Fig. 1, this means that, in the three phase system, the contributions from each separate interface (carbon-air, carbon-water and water-air) can be added to provide the total scattering signal. Note that the carbon fibers in a GDL are randomly oriented and thus we show in Fig. 1 also randomly chosen points with the distance ξ_{GI}. In case anisotropic systems are analysed with vertical gratings, only points that can be connected by horizontal lines should be considered.

To obtain a high contrast between a DF image of the dry GDM and a DF image of the GDM with water in the pores, it is advantageous to operate the fuel cell with D_2 (producing D_2O) instead of H_2 (producing H_2O). The reason for this is that the scattering length density contrast ΔSLD_{C-Air} is almost the same as ΔSLD_{C-H_2O}, while there is a significant difference between ΔSLD_{C-Air} and ΔSLD_{C-D_2O} (see Ref. 60 for details). Another important parameter to be considered carefully to obtain a good contrast-to-noise ratio (CNR) in DF images is ξ_{GI}.

Noise in DF images depends on the neutron flux reaching the detector (determined by the flux of the beam line and transmission of
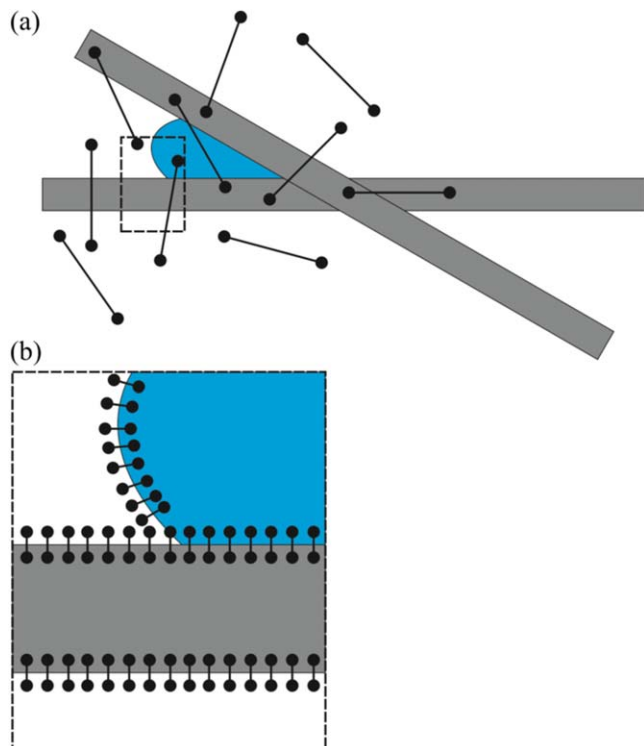
Figure 1. Illustration of three phase system consisting of carbon fibers, air and water. The correlation length of the grating interferometer ξ_{GI} is shown in comparison to the characteristic structure sizes. (a) ξ_{GI} is longer than the characteristic structure size (i.e. carbon fiber diameter) and the probability is high that several interfaces are within the distance ξ_{GI}. In this situation, the analysis of a three phase system is complicated, because the scattering signal is not proportional to the amount of interfaces. (b) ξ_{GI} is considerably shorter than the characteristic structure sizes and thus the scattering signal is proportional to the amount of interfaces.

the sample), on the measured open beam visibility (V_0) of the nGI setup, and on the DF value measured for a specific sample. A low scattering contrast (high DF value) or a high contrast close to saturation (DF value close to zero) obviously results in a low CNR. For low DF values the relative uncertainty increases due to the relatively higher impact of statistical noise on the fitting algorithm as discussed in reference.[77] In addition, DF values approaching zero are also affected by a systematic bias when common fitting algorithms are used.

   As most fuel cell test fixtures are a few centimeters thick, it is not possible to put the center of the fuel cell (GDM and catalyst coated membrane) very close to G2. Thus, it is important to choose p_2 and λ such that ξ_{GI} is in the optimal range to yield a DF value which is sufficiently low but does not saturate the signal (values close to 0), when L_S has a value of a few centimeters. In addition, $\sum_S$ depends on the square of λ, which also needs to be considered to design an optimal nGI for fuel cell applications. It is more challenging to fabricate gratings suitable for short wavelength neutrons as their penetration depth in absorbing material (e.g. gadolinium) is larger and thus, high aspect ratios for absorption gratings are required. This is why common nGI setups are usually designed for long wavelengths (>4 Å). Depending on the spectrum of the beamline, it can be advantageous to measure at a shorter wavelength to benefit from a higher flux. In addition, it has to be evaluated whether white beam measurements result in a higher CNR compared to experiments performed with monochromatic beams (e.g. with a velocity selector or a double crystal monochromator). In this case, the optimal gratings should be designed for the intensity weighted average wavelength of the beam line.

   None of the previously reported nGI setups provided a flux and open beam visibility (V_0) sufficiently high to reach a CNR that allows

DF imaging with acquisition times interesting for fuel cell operando experiments. The requirement to place the center of the cell at a sufficient distance from G2 limits the range of accessible values for ξ_{GI}. Conventional nGI setups have a large distance (a few meters) between G0 and G1, while the distance between G1 and G2 is commonly in the range of a few centimeters.[61,67,70,78] The distance can be increased by using higher Talbot orders but this goes along with a decreased visibility.[79] Donath et al.[80] elaborated the theoretical background for a symmetric X-ray grating interferometer (xGI), with a larger distance between G1 and G2 and Kim et al.[71,81,82] demonstrated the feasibility of a symmetric nGI. We designed a symmetric nGI with parameters (grating periods, wavelength) that allow us to measure with a ξ_{GI} that yields a high CNR for the DF value of two GDM mounted inside a fuel cell test fixture. Another advantage of the symmetric setup is the larger period for G2 compared to conventional setups.[61] The most frequently used fabrication method for conventional setups with a G2 having a small period (e.g. 4 μm[61,67,70,78]) is gadolinium evaporation onto a silicon grating. A larger period of G2 allows to use different fabrication methods such as, for example, laser ablation of gadolinium. The setup was optimized for a wavelength of 3.5 Å, which is the intensity weighted average wavelength of the ICON beam line where the experiments were performed. Thus, we could measure with a white beam and benefit from a high flux, which is advantageous to reach a high CNR.

Experimental

   Gratings fabrication.—DF images were acquired with an nGI setup, which consisted of three gratings: a source grating (G0) and an analyzer grating (G2) with absorbing lines as well as a phase grating (G1). The nGI setup was symmetrical with a distance of 44.5 cm between G0 and G1 and the same distance between G1 and G2, corresponding to the first Talbot order. G1 was manufactured by dry etching into a silicon wafer. The bars had a height of 43.28 μm, and were designed to introduce a π-phase shift to neutrons with a wavelength of 3.5 Å. G1 had a duty cycle of 50% and a period of 25 μm. The two absorption gratings (G0 and G2) were manufactured by sputtering gadolinium with a thickness of 16 μm onto quartz wafers. Subsequently, gadolinium was removed by laser ablation to form the grating pattern. Two sets of G2 and G0 were produced, which differed by the period which was either 25 μm or 26 μm and the duty cycle which was either 37% or 25% (see Table I) at the half of the grating height (see Fig. 2).

   Symmetric nGI setup variants.—All experiments were performed with the same G1 grating (25 μm period, 50% duty cycle). For the absorption gratings (G0 and G2), we used periods of 26 μm or 25 μm and either a 16° or 0° rotation angle with respect to the axis perpendicular to the beam (x-axis) as displayed in Fig. 3 and summarized in Table I. Rotating a grating with 26 μm period by 16° results in an apparent period of 25 μm, which can be finely adjusted by the rotation angle. Conventional nGI setups with a large distance (a few meters) between G0 and G1 are usually designed with a G0 that can be rotated with respect to the x-axis in order to match the geometrical requirements.[61] However, the rotation introduces a varying distance between G0 and G1 along the x-axis, which

Table I. Grating parameters for the three nGI setup configurations used in the experiments.

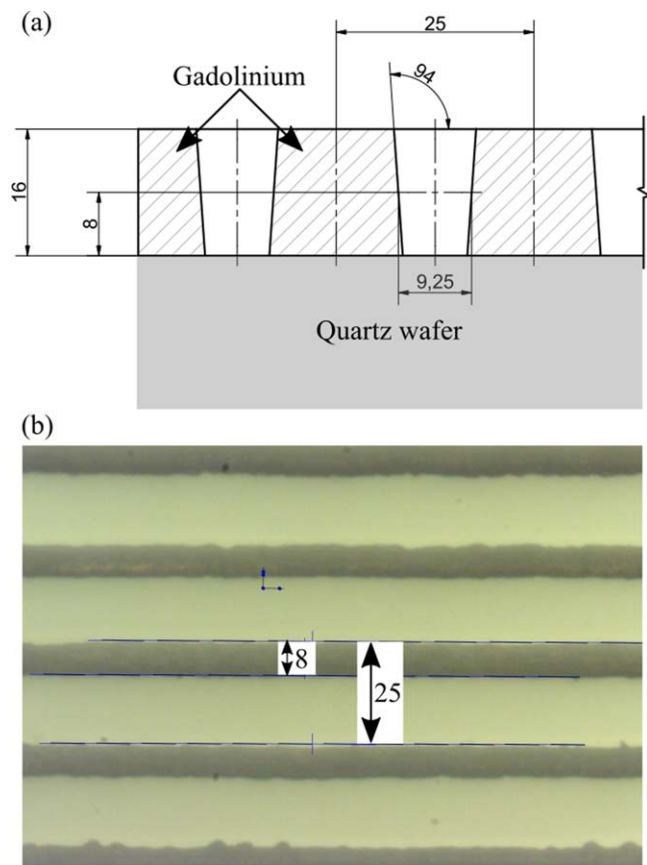|		Period μm	Duty cycle %	Rotation angle (α) °
setup1	G0	26	37	16
	G2	25	37	0
setup2	G0	25	37	0
	G2	25	37	0
setup3	G0	26	25	16
	G2	26	37	16

(a)

(b)

Figure 2. (a) Schematic of cross section of grating fabricated by laser ablation of gadolinium sputtered previously onto a quartz wafer. (b) Optical microscope image of grating with 25 μm period. The dark lines are gadolinium free and have a width of 8 μm at the gadolinium/quartz wafer interface for a grating with 37% duty cycle at half height of the gadolinium layer.

influences the visibility in a symmetric setup with a comparably small distance between G0 and G1 as will be discussed in the "Results and Discussion" section.

Fuel cell operation.—The fuel cell used for the experiments had an active area of 13.2 cm^2 (2.2 cm × 6 cm). A parallel flow field was used on the anode side, and an interdigitated flow field on the cathode side. Both flow fields were machined in aluminum and included a gold coating with 5 μm thickness to prevent corrosion. The flow fields had 11 gas channels (1 mm wide, 0.5 mm deep) separated by 1 mm wide ribs. The two compression bodies (test fixture) were made of aluminum blocks with a thickness of 40 mm and a cavity of 20 mm in the region of the active area which is an advantage for neutron transmission. The catalyst coated membrane (CCM) was a Primea 5710 (W.L. Gore & Associates) membrane with cathode Pt loading of 0.4 mg cm^{-2} and anode Pt loading of 0.1 mg cm^{-2}. The anode GDM was a Freudenberg H23 C6 with a commercial microporous layer (MPL). The base material for the cathode GDL was of type Freudenberg H23 and it was in-house modified to feature patterned wettability.[83,84] The pattern had 500 μm wide hydrophilic lines separated by 940 μm wide hydrophobic regions. A MPL was also applied in-house to the cathode GDL (see Ref. 84 for the synthesis details). For simplicity, we call the GDL with MPL hereafter gas diffusion media (GDM). Both GDM had an initial thickness of 220 μm and were compressed by 25% to a thickness of 170 μm when mounted in the fuel cell. The cell was operated in counter flow at 40 °C without humidification of the feed gases. The gas fed at the cathode was air with a

stoichiometry of 1.4 and the anode was fed with D$_2$ or H$_2$ with a stoichiometry of 2.5. For the operando experiments, the current density was 1 Acm^{-2}. Further experiments were conducted with a static water distribution. In this case, the cell was first operated for 10 min to generate water. Subsequently, water was partially removed by flowing dry gas in the anode with 1000 mlmin^{-1} during two periods of 5 min. Images were acquired for 20 min at three different time points (before the first drying, between the two dryings and after the second drying).

Image acquisition and processing.—The experiments were performed at the ICON beam line[85] of the Swiss Spallation Neutron Source (SINQ). A 200 μm thick ^{6}LiF/ZnS scintillator was used to convert neutrons to photons. Images were acquired with a CCD camera (IKON-L) combined with a 100 mm optical lens (Zeiss Makro Planar T100/2), resulting in a field of view of 93 × 93 mm^2 and a pixel size of 48 μm. The exposure time was set to 10 s. Different neutron apertures were used with diameters of 10, 20 or 40 mm and the cell center was placed at a distance of 85 mm from the detector and 7.53 m from the aperture. Hence, the geometrical blurring was approximately 0.22 mm with an aperture of 20 mm and 0.45 mm with an aperture of 40 mm, respectively. The phase stepping was provided by moving G0. In the "standard" scan strategy, G0 was moved in constant direction over a distance corresponding to one period using either 14 or 21 images per period.

Additionally, we introduced a golden ratio scan strategy for the phase stepping. Similar to the golden ratio acquisition strategy in a tomography, the half of the G0 period is divided by the golden ratio (1.618) to obtain the phase stepping distance. When the movement has exceeded one full period, the grating is driven back by the distance corresponding to one G0 period and the procedure is repeated. This scan strategy, popular for time resolved tomographies,[86] ensures an optimal distribution of the grating positions over a period for an arbitrary *a posteriori* choice of the analysis interval.

The total exposure time (number of phase step images * exposure time) for each data set presented will be mentioned in the Results and Discussion part. It must be noted that the total image acquisition time, including motor driving for the phase-steps and image read out time, is higher than the total exposure time.

For some experiments, a velocity selector was used to produce a monochromatic beam with a target wavelength of 3.5 Å ($\Delta\lambda/\lambda$ = 15%), while other experiments were performed with the full white beam. The intensity weighted average wavelength for the spectrum of the ICON beam line is 3.5 Å. Thus, ξ_{GI} is similar for experiments performed with white beam and with velocity selector and amounts to 1.2 μm. The range of ξ_{GI} is 0.3–2.7 μm for the wavelength range of the white beam. Thus, ξ_{GI} is much smaller than the average structure sizes present in the GDL. DF images, attenuation contrast images and visibility maps were obtained with the open source software TaPy.[87] The following steps are performed on each phase-step image: pixel-wise subtraction of camera background, outlier removal to filter out bright spots which are for example produced when γ-Rays hit the chip of the detector, 2 × 2 binning and correction for beam intensity fluctuation by normalizing images by a non-changing area outside of the grating areas. TaPy includes an algorithm using efficient matrix operations[88] to fit the amplitude and mean value of the intensity modulation in each pixel for open beam and sample images.

The transmission images of the fuel cell with water were divided by a dry image of the cell and the Beer–Lambert law was used to calculate the water thickness. The effective attenuation coefficient ($\sum_{H_2O}$ = 4.96 cm^{-1}) was calculated for the white beam spectrum of the ICON beam line with reference cross section data from reference.[89] DF images of the water filled cell were referenced by subtracting the image of the dry cell. Here after we refer to the DF value difference between the water filled and dry cell as DFVD$_{(wet-dry)}$. To reduce noise, Gaussian smoothing with σ = 2
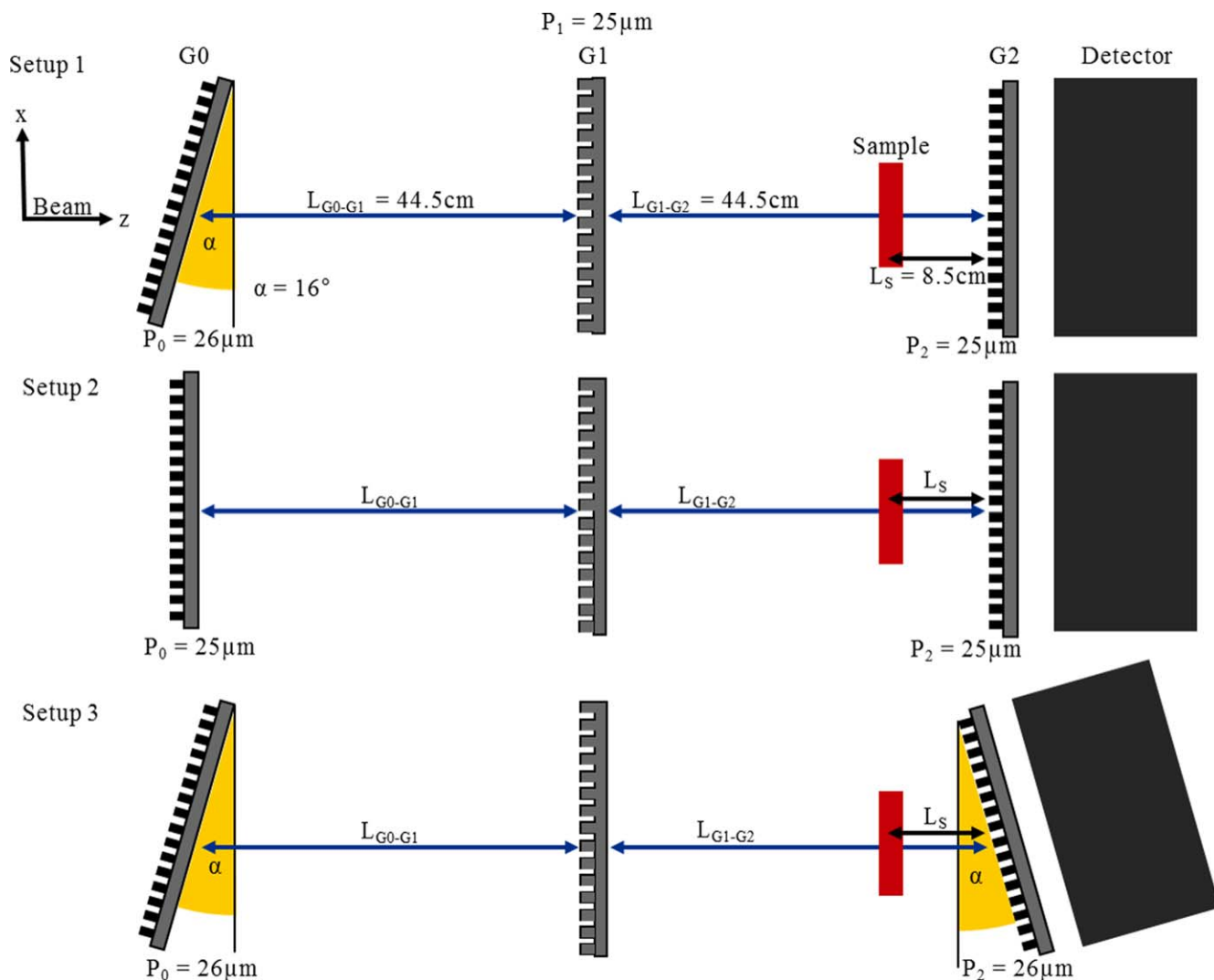
Figure 3. Schematic of top view onto symmetric nGI setup configurations used in the experiments.

and a kernel of 3 × 3 was applied in some cases to DF images. This is stated in the figure caption in cases where applicable.

Results and Discussion

Visibility with improved fabrication method.—Figure 4 shows the visibility maps measured with the three different setup configurations with an aperture of 20 mm and monochromatic beam (3.5 ± 0.26 Å) (top row) and with an aperture of 40 mm and white beam (bottom row). For all setups the visibility is higher with the monochromatic beam with the wavelength for which the gratings are optimized. With setup 1 (Table I and Figs. 3a and 3d), a high visibility (51%) was measured in the center of the field of view, but visibility decreased substantially towards the sides. The low visibility at the sides is explained with the rotation around the *x*-axis of G0. The distance between G0 and G1 at the borders is not the same as the distance between G2 and G1. Setup 2 delivers a lower but more homogeneous visibility (46%) compared to setup 1. The stripe with low visibility at the left side is due to defects (mismatch of period) in one of the absorption gratings. The periodic structures (vertical lines) appearing in the visibility maps may be the result of remaining period mismatches between G0, G1 and G2. However, they do not seem to affect the DF images, as the division by the open beam visibility removes them entirely (see Eq. 2). With setup 3, we measured a homogeneous visibility over the whole field of view, and the value (57%) is higher than the peak value of setup 1. The

visibility is very sensitive to small mismatches in the period of the three gratings. For setups 1 and 3, the period of G0 was fabricated 4% larger than the target period and the grating was placed with an angle of 16° in respect to the axis perpendicular to the beam (*x*-axis in Fig. 3) to achieve an apparent period of 25 *μ*m. The apparent period is calculated by simply multiplying the physical period with the cosine of the rotation angle. With a design rotation angle of 16° one can easily fine-tune the apparent period by adjusting the rotation angle. Thus, it is possible to compensate for a period mismatch between G0 and G1 possibly introduced due to fabrication inaccuracies, which explains the higher visibility reached. This is not feasible when the fabricated period of all three gratings is the same and the gratings are placed without rotation around the *x*-axis. Because the cosine is not a linear function, much larger changes of the rotation angles are needed to compensate for small period mismatches between G0 and G1 when the design rotation angle for G0 is 0°. With setup configuration 3, aperture = 20 mm and monochromatic beam, we measure a homogenous visibility of nearly 60%. This is a substantial improvement compared to visibility values (defined by Eq. 1) of 20–30% reported previously for other nGI setups,[61,70,71] which used a G2 fabricated by gadolinium evaporation. Laser ablation of gadolinium from wafers bears the advantage of a better defined absorption pattern compared to gadolinium evaporation. We do not achieve a perfect absorption profile, because the laser pulse is most intense in the center, which results in a trapezoid cross section as shown schematically in Fig. 2a. However,
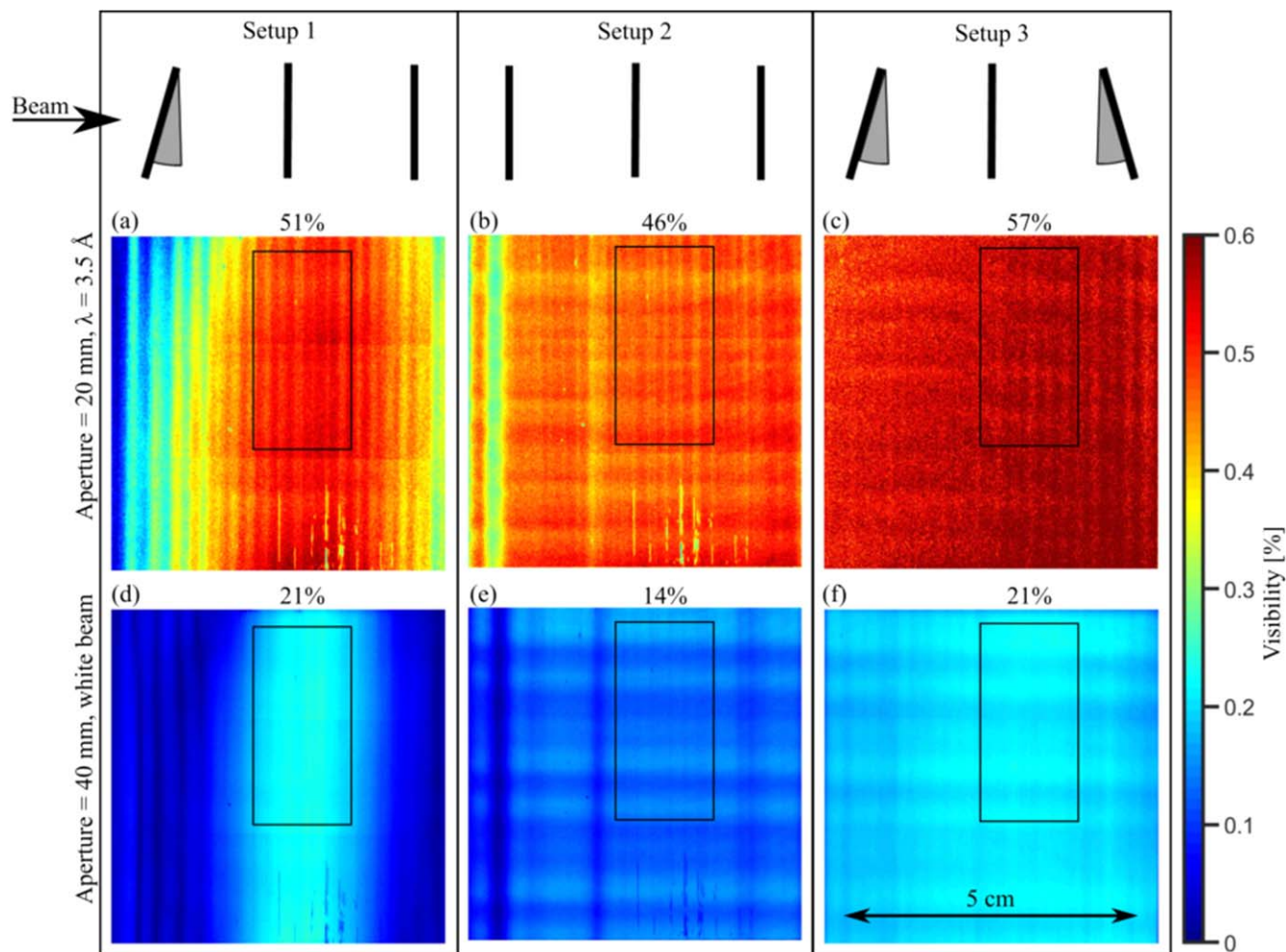
Figure 4. Visibility maps displayed with a color code. The mean value, displayed on top of the image, was calculated using the region highlighted with the black rectangle. Top row: aperture = 20 mm and monochromatic (3.5 ± 0.26 Å). Bottom row: aperture = 40 mm and white beam. (a), (d) setup 1, (b), (e) setup 2 and (c), (f) setup 3.

the absorption pattern is much closer to the optimal case of a rectangular pattern, which was predicted by Harti et al.[79] to result in a significant improvement of visibility. The use of laser ablation was possible, because a larger period for G2 compared to other reported setups can be used for a symmetric setup. For small G2 periods, the trapezoid shape of the grating obtained with laser ablation (Fig. 2a) would severely affect the transmission of the grating.

Seki et al.,[90] reported visibility values of 50% at 5 ± 0.055 Å using a G2 fabricated by gadolinium evaporation, but the area of the grating was only 20 × 20 cm². Other groups[91,92] have recently reported about improved methods for the fabrication of absorption gratings (G2), which are expected to increase visibility compared to previously reported setups.

Figure 5 compares for setup 3 the visibility and beam intensity measured with an aperture of 10, 20 and 40 mm with monochromatic and white beam. The larger the aperture, the lower the visibility, because a period mismatch between G0 and G1 has a larger effect if a higher number of source lines contribute to the signal in a given point. On the other hand, the flux increases linearly with the aperture area. The highest increase in flux is achieved by measuring with white beam instead of monochromatic beam (an increase of factor 25 for the same aperture). The visibility decreases by using a white beam, because the set-up was optimized for a single wavelength. However, the figure of merit *FOM* to obtain a high CNR for images is described by Eq. 5 and is strongly influenced by the available neutron flux, *I* as shot noise decreases proportionally to the square root of the flux:

$$FOM = V_0 \sqrt{I}. \quad [5]$$

Measuring with white beam and an aperture of 40 mm yields a figure of merit which is 3.5 times higher than for measuring with an aperture of 20 mm and monochromatic beam. This increase in figure
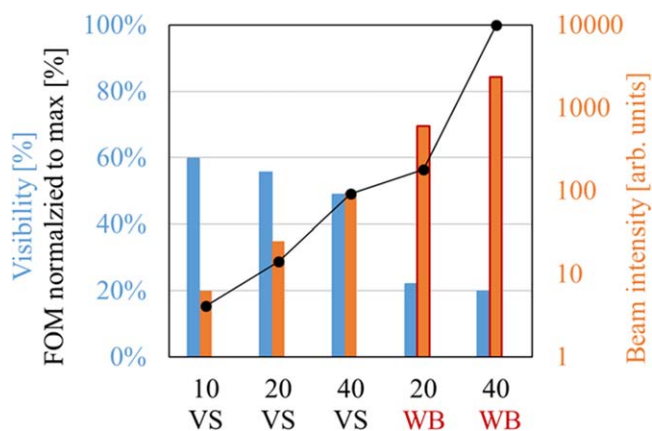

Figure 5. Visibility (blue bars, left *y*-axis) and beam intensity (orange bars, right *y*-axis) measured with an aperture diameter of 10, 20 and 40 mm with velocity selector (VS) and white beam (WB). Figure of merit (FOM) is shown with black dots (left *y*-axis).

of merit means that the contrast to noise ratio (CNR) is increased by a factor 3.5 for a given exposure time, or that the exposure time can be reduced by a factor of 12.25 while keeping the same CNR.

Microstructural inhomogeneities of the dry GDM.—Figure 6 shows DF images and attenuation contrast images of a dry fuel cell. The DF contrast is larger for the active area compared to areas where only the test fixture of the cell (aluminum) is in the beam (Figs. 6a and 6c). This strong DF contrast is generated by neutrons, which are scattered at the microstructure of the cathode and anode GDM. The transmission value (Figs. 6b and 6d) scales with the thickness of neutron attenuating materials in the beam. The highest transmission value is measured in the region of the active area, because the test fixture is manufactured with a cavity in this region. With both imaging methods, the strongest contrast is measured for the footer, which is made from glass fiber loaded polyphenylensulfid (PPS) and generates both attenuation and scattering contrast as it contains hydrogen and microstructures. In the attenuation contrast image acquired with setup 3 (Fig. 6d), we can observe shadows at both ends of the active area, because the cell is rotated by 16° compared to the axis perpendicular to the beam. In the DF images acquired with setup 3 (Fig. 6c), the shadow is only visible at the right border. The reason for this is that, due to the rotation of the cell, the aluminum border of the test fixture around the cavity is at one side closer to G2 than at the other. Illustrative figures are shown in supplementary information (Figs. S1 and S2 is available online at stacks.iop.org/JES/167/064509/mmedia). The distance between sample and G2 influences ξ_{GI} and thus the DF contrast. In future experiments, the nGI can be optimized in such a way that no rotation of the cell is necessary or the cavity can be adapted to avoid this

shadow artifact. Hereafter, we focus on the region of interest highlighted in Figs. 6a and 6c with the turquoise rectangle.

The image in Fig. 7a was acquired with an aperture diameter of 40 mm and the image in Fig. 7b with an aperture diameter of 20 mm. From both images and from the blue line profiles (average of pixels in horizontal direction), it is visible that there is a regular pattern of the DF value. The period of this pattern corresponds to the sum of the widths of channel and rib (2 mm). The DF value is about 0.01 (2.7%) higher for rib areas compared to channel areas. This confirms that the DF contrast is sensitive to small microstructural changes in the GDM. A higher compression under the flow field ribs reduces the porosity and thus air gaps between fibers. As a consequence, the surface area between carbon and air is reduced, which results in less scattering sources and thus a higher DF value is measured. The red line profiles (average of pixel in vertical direction) look different for the two images. While there are no special features visible in the red line profile shown in Fig. 7a, such are clearly visible in the image and red line profile in Fig. 7b. There is a regular structure of thin lines and the profile given below the image shows a regular pattern of the DF value. The period of this pattern is about 0.54 mm and corresponds to the period of the line structure of the Freudenberg H23 GDM (see Fig. S3 in supplementary information). The reason why this structure is not visible in the image acquired with an aperture of 40 mm is geometrical blurring, which amounts to 0.45 mm. With an aperture of 20 mm, the geometrical blurring is only half of this and thus smaller than the period of the structure. For the experiments reported here, geometrical blurring was comparably large because we placed the center of the cell 85 mm away from the detector. The compression body had a thickness of 40 mm and we could have placed the cell closer to the detector. However, a smaller
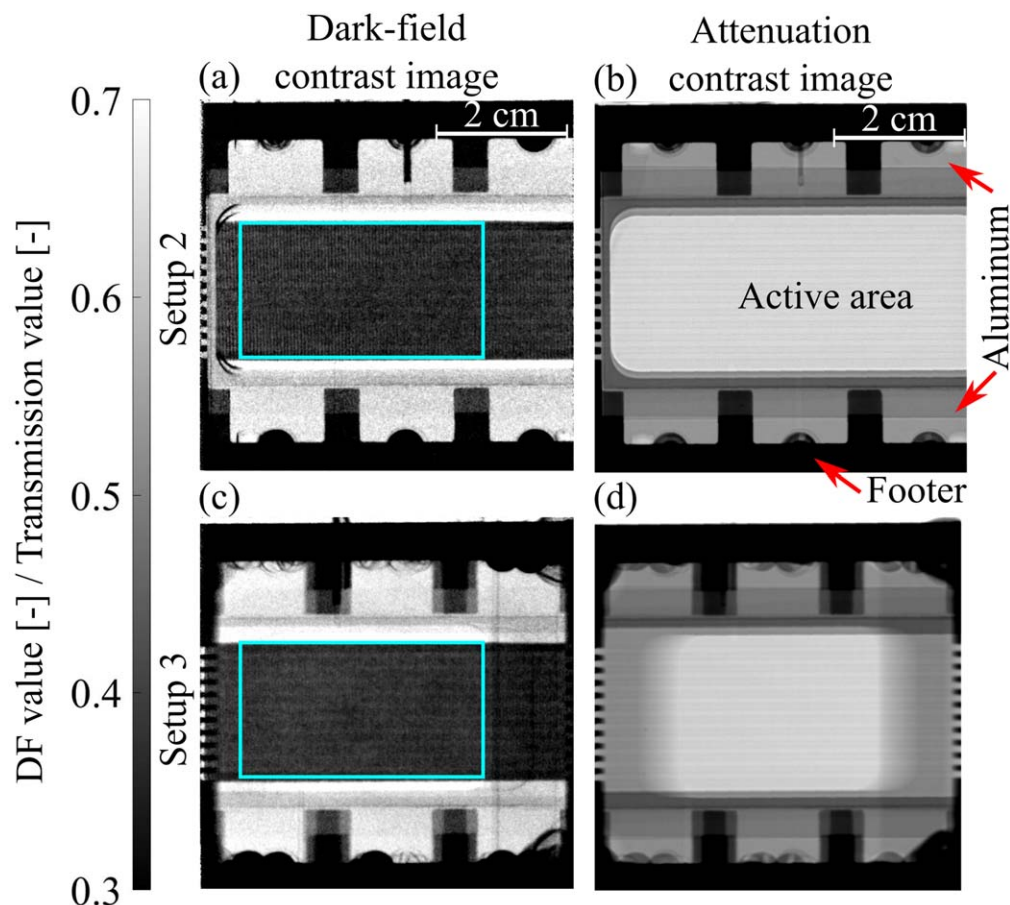

Figure 6. Comparison between DF images (a), (c) and attenuation contrast images (b), (d) acquired with setup 2 (a), (b) and setup 3 (c), (d). Turquoise rectangle highlights region of interest shown in Figs. 7, 9, 11 and 12.
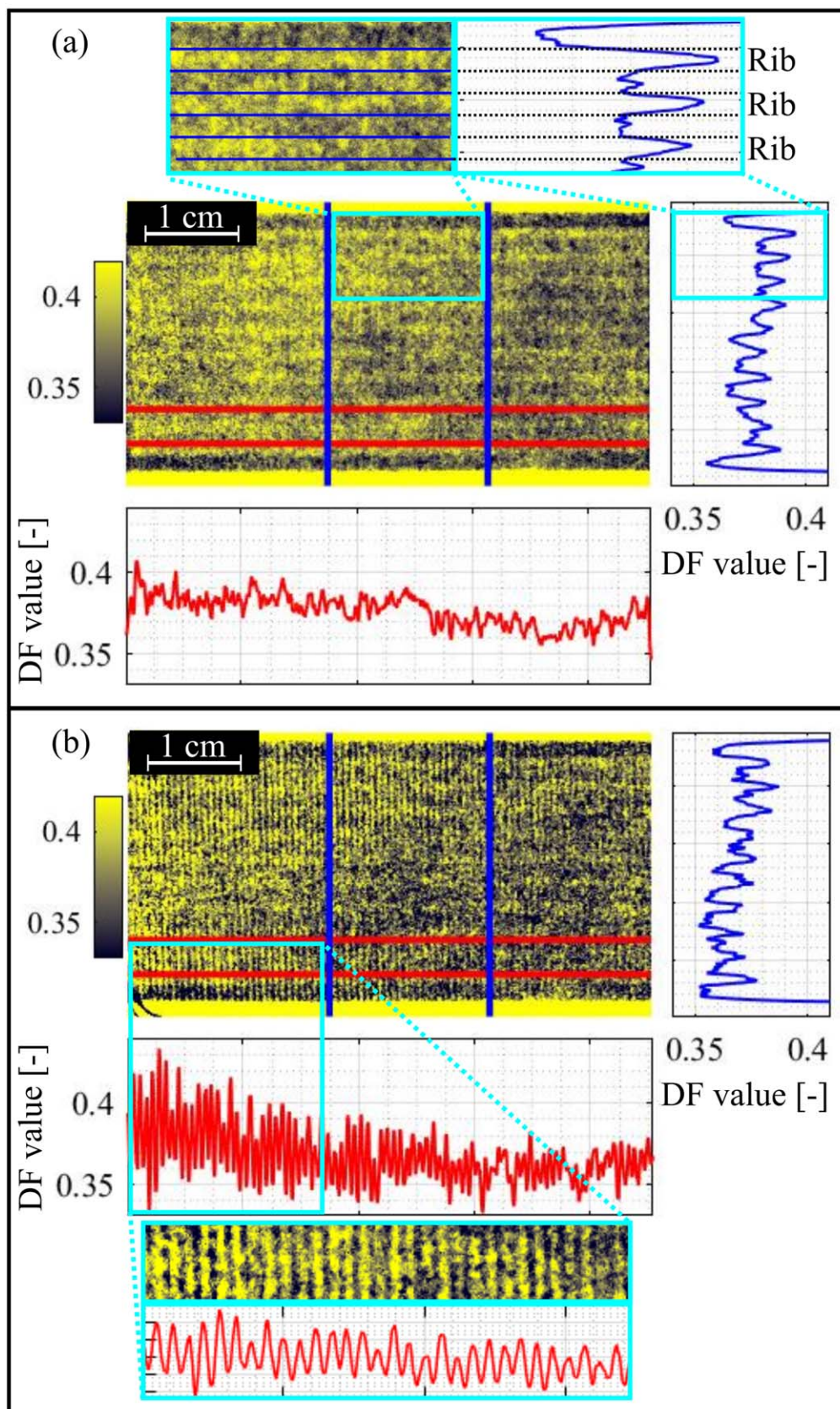
Figure 7. DF images of dry GDM mounted in the fuel cell test fixture acquired with a total exposure time of 20 min. Images are shown with a color code. (a) aperture = 40 mm. (b) aperture = 20 mm. Red line profiles show DF values averaged in vertical direction and blue line profiles show DF values averaged in horizontal direction. Inserts show small GDM areas and the corresponding part of the line profiles magnified.

distance to G2 would have resulted in a smaller ξ_{GI} and thus less DF contrast and smaller CNR. In case the goal for future studies is to investigate microstructural inhomogeneities of GDM with higher spatial resolution it is important to design the nGI accordingly. For the rest of this publication, we present results based on images acquired with an aperture of 40 mm, because for the same exposure time a higher CNR is obtained thanks to an increased neutron flux.

Visualization of water in GDM—Static distribution after fuel cell operation.—To analyze the water distributed in pores of different regions in the GDM, we used a mask to treat four "domains" separately. The four domains are rib/channels overlapping with hydrophilic/hydrophobic areas as illustrated in Fig. 8.

Figure 9 compares the DF image of the dry fuel cell (Fig. 9a) to the one obtained after the cell was operated for 10 min with D_2 (Fig. 9b) to produce D_2O. Further, we compare the DF value difference between wet and dry cell ($DFVD_{(wet-dry)}$) displayed in Fig. 9c to the H_2O thickness shown in Fig. 9d. The latter is calculated based on the attenuation contrast image and was acquired after 10 min of operation with H_2. The water distribution is similar after operation with D_2 and H_2, but the H_2O thickness image suffers from less noise, because the attenuation coefficient of H_2O is much larger than the one of D_2O. For a detailed discussion on the

comparison between attenuation contrast and DF images of GDM filled with D_2O/H_2O, see our previous publication.[60] The line profiles below the images show the average pixel values for rib (red) and channel (black) regions and those to the right of the images display the average pixel values for hydrophilic (blue) and hydrophobic (yellow) regions. As above for Fig. 7a, we can observe for the image of the dry cell a higher DF value for rib compared to channel regions. For hydrophilic and hydrophobic regions, the DF value is the same (Fig. 9a). The DF image of the fuel cell containing D_2O reveals that the DF value varies more between channel and rib than for the dry cell (Fig. 9b). In addition, the DF value is higher for hydrophilic regions compared to hydrophobic regions, especially for the rib regions (red line profile). The DF value of the rib regions shows a pattern with a period of 1.44 mm, which corresponds to the period of the hydrophilic/hydrophobic line pattern. Details about this pattern are discussed later on the basis of Fig. 11. We obtain a positive $DFVD_{(wet-dry)}$ for the rib regions and a negative $DFVD_{(wet-dry)}$ for the channel regions (Fig. 9c). The water thickness image and corresponding line plots show that there was about 50 μm of water in the rib region of the GDM (Fig. 9d) and it is visible, that some channels are more filled by water than others, with the average value ranging between 50 μm and 100 μm. There are no important variations of the $DFVD_{(wet-dry)}$ between the different channels
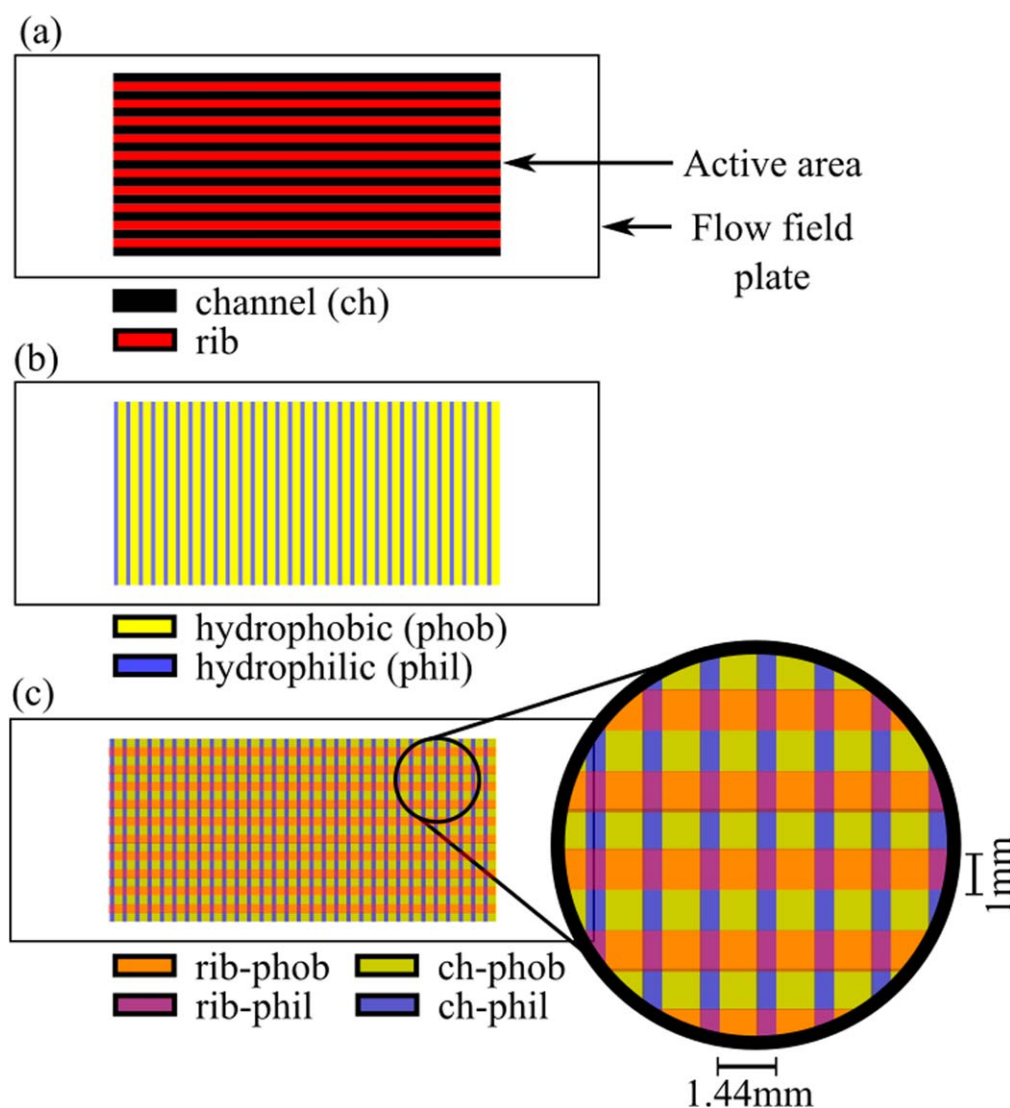

Figure 8. Mask for the four domains in the GDM. (a) Channel/rib, (b) hydrophobic/ hydrophilic lines, (c) channel/rib overlapping with hydrophobic/hydrophilic lines.
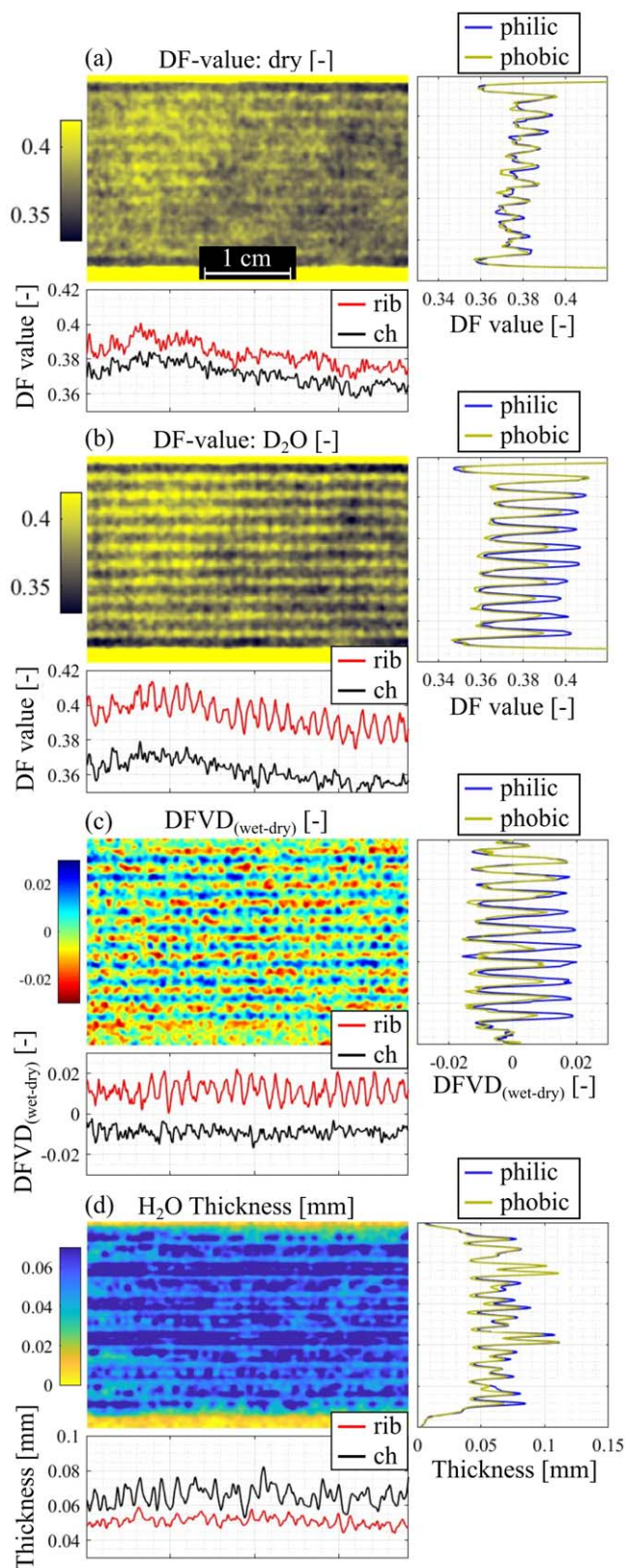
Figure 9. Static water distribution in fuel cell after 10 min of operation. (a) DF image of dry fuel cell, (b) DF image of D_2O-filled fuel cell, (c) $DFVD_{(wet-dry)}$, (d) H_2O thickness image calculated based on the attenuation contrast image. Images were acquired with a total exposure time of 12 min. Red (rib areas) and black (channel areas) line profiles show values averaged in vertical direction and blue (hydrophilic) and yellow (hydrophobic) line profiles show values averaged in horizontal direction. DF images are shown with Gaussian smoothing, but line profiles were evaluated based on the unfiltered images.
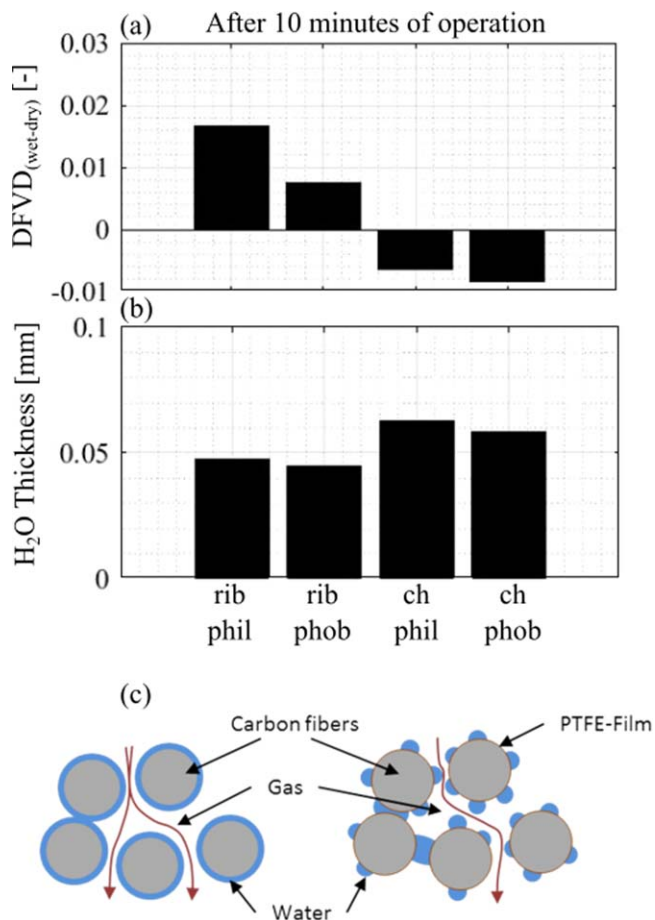

Figure 10. (a) $DFVD_{(wet-dry)}$ and (b) H_2O thickness measured for the four domains of the GDM (rib & hydrophilic, rib & hydrophobic, channel & hydrophilic, channel & hydrophobic). (c) Schematic of water microstructure in hydrophilic GDL (left) and GDL with hydrophobic coating (right) reprinted from.[17]

observable. This behavior is expected: most of the water clusters present in flow field channels are expected to have dimensions (length and width) to which the DF contrast is not sensitive.

Figure 10 is a summary of the observations presented in Figs. 9c and 9d. It displays the $DFVD_{(wet-dry)}$ and the water thickness for the four domains. We measure a positive $DFVD_{(wet-dry)}$ in rib and a negative $DFVD_{(wet-dry)}$ in channel regions. As elaborated above in the theoretical background, we measure with a small ξ_{GI} compared to the structure sizes in a partially water filled GDM. Thus, we can assume that the DF value is mainly proportional to the amount and kind of media interfaces present in the GDM (see Fig. 1).

As shown in detail in reference,[60] it is expected and was experimentally proven that a positive $DFVD_{(wet-dry)}$ is obtained, when most of the pores are filled with heavy water, because the ΔSLD_{C-D_2O} is much smaller compared to ΔSLD_{C-Air}. Replacing C-air interfaces with C-D_2O interfaces results in a smaller DF contrast (higher DF value). However, the $DFVD_{(wet-dry)}$ was shown to decrease for partially heavy water filled GDM, as additional D_2O-air interfaces increase the DF contrast. The results presented in Fig. 10a indicate, that the effect of a reduced DF contrast (form C-D_2O interfaces replacing C-air interfaces) is overcompensated by an increased amount of air-D_2O interfaces and thus the $DFVD_{(wet-dry)}$ is negative. Such a situation can be explained by the presence of a large number of small droplets present in the GDM, which have a large surface area and contribute to the interface air-D_2O. Although the $DFVD_{(wet-dry)}$ for rib and channel regions has a different sign, we can still observe a difference between hydrophobic and hydrophilic areas in both cases (Fig. 10a). The

DFVD$_{(wet-dry)}$ for hydrophilic areas under the rib is more than twice as high compared to hydrophobic areas under the ribs. On the contrary, based on the attenuation contrast image, we calculate a water thickness that varies very little (less than 5 μm or 10%) between hydrophilic and hydrophobic areas in the rib region. Water droplets distributed in hydrophobic porous material with a larger contact angle are expected to form more discrete droplets while water will tend to form films on the surface of hydrophilic material as illustrated schematically in Fig. 10c. Therefore, the specific water structure can lead to a higher amount of air-D$_2$O interfaces in hydrophobic materials, resulting in a reduction of the DF value (stronger DF contrast). In channel regions, a similar change of DF value between hydrophilic and hydrophobic regions is observed, but with a lower magnitude. This is most likely explained by the fact that less water is present in GDM areas overlapping with channels compared to those overlapping with ribs.

In summary, the fact that the DFVD$_{(wet-dry)}$ does not scale proportionally with the amount of water present in the pores of the GDM represents both a challenge and an opportunity. The challenge is that depending on the GDM material and water saturation one might encounter the situation where zero difference is measured even when water is present. On the other hand, DF imaging represents an opportunity, as it is sensitive to the microstructure of water, because the surface area is different for small droplets compared to water films. Thus, DF imaging allows gaining information about the water distribution in fuel cells beyond simple quantity mapping as obtained with attenuation contrast imaging. To obtain a fundamental understanding of the link between the DF value and the microstructure of water droplets distributed in a specific GDM, DF imaging results should be compared to the results of X-ray tomography studies in the future. Obtaining quantitative information on the water distribution could also be achieved by calibrating the DF signal for a specific GDM and water distribution either by using neutron imaging with special purging procedures or analyzing the water thickness with the cell membrane parallel to the beam.

Visualization of water in GDM—Drying steps.—Figure 11 displays line profiles and bar plots for the DFVD$_{(wet-dry)}$ and water thickness evolution during a drying procedure. Step 1 corresponds to the images after the fuel cell was operated for 10 min (either with D$_2$ or H$_2$ as for the data presented above). Subsequently, the fuel cell was dried in two steps (step 2 and step 3) by flowing dry nitrogen at the anode side for 5 min. In the plot of the line profiles, it is indicated with dashed vertical lines where the hydrophilic lines are expected to be located by knowing the period of the pattern. In the rib areas we can observe the presence of the hydrophobic/hydrophilic pattern for the DFVD$_{(wet-dry)}$ during all three steps, but in the channel area noise obscures the pattern (Fig. 11a). The water thickness measured from attenuation contrast varies clearly between hydrophilic and hydrophobic rib regions after the first drying (step 2), while before drying no clear pattern was observed. In the channel areas there is no clear pattern for all three steps. The water thickness image acquired after the first drying (step 2) shows that there is still some water left in channels at the left side. In regions where the channels are dry, the pattern of water mostly accumulated in hydrophilic lines can be observed. It appears that the pattern becomes clearly visible in the water thickness image only after drying when the channel water at the anode is removed.

Visualization of water in GDM—operando measurements.—Figure 12 displays the DFVD$_{(wet-dry)}$ and water thickness image averaged over 60 min of operation and the corresponding line profiles. The water content in the GDM increases during the first few minutes of operation, after which an equilibrium is established between water generation and water transport to the channels. Therefore, once this equilibrium is reached the GDM water content is not expected to change dynamically when operation parameters (current density, relative humidity, temperature, gas pressure) are constant.
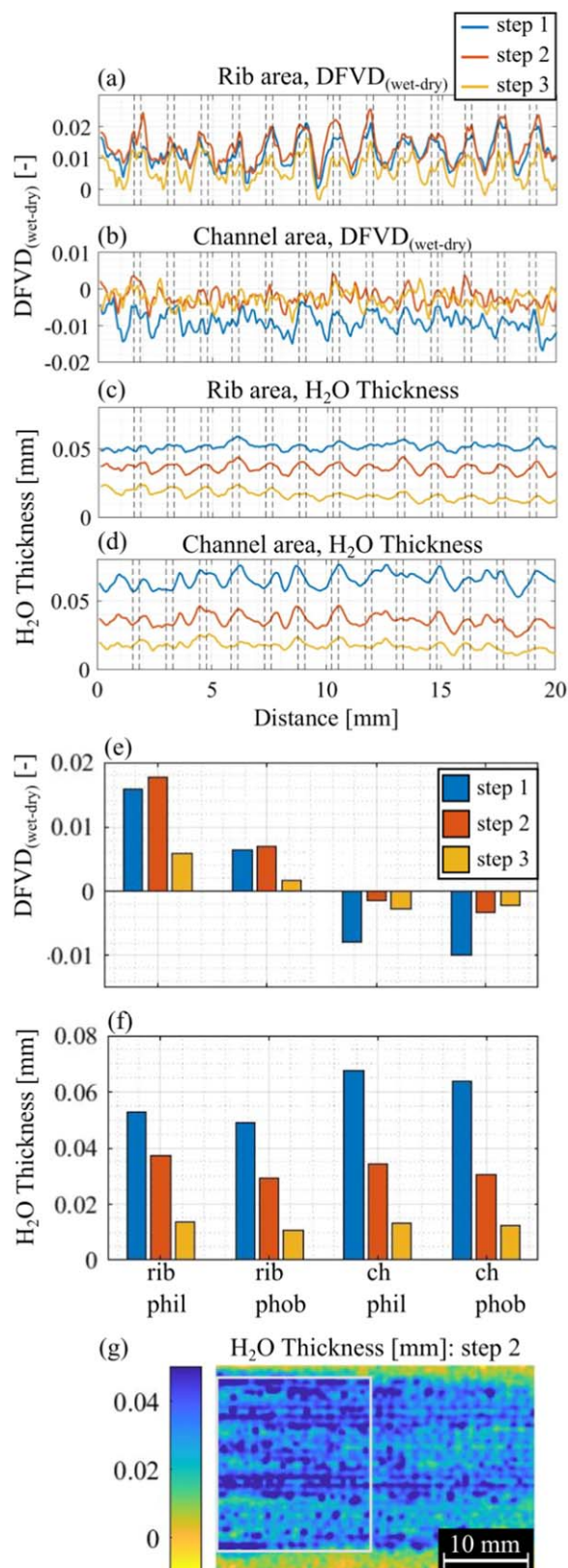

Figure 11. Line profiles for DFVD$_{(wet-dry)}$-images acquired with a total exposure time of 12 min after 10 min of operation (step 1) and after two drying steps (step 2 and step 3) for (a) rib and (b) channel areas and H$_2$O thickness in (c) rib and (d) channel areas. Bar plots depict the average of the four domains for (e) DFVD$_{(wet-dry)}$ and (f) H$_2$O thickness. (g) H$_2$O thickness image acquired after first drying (step 2). Grey rectangle highlights region of interest for which line profiles are shown.
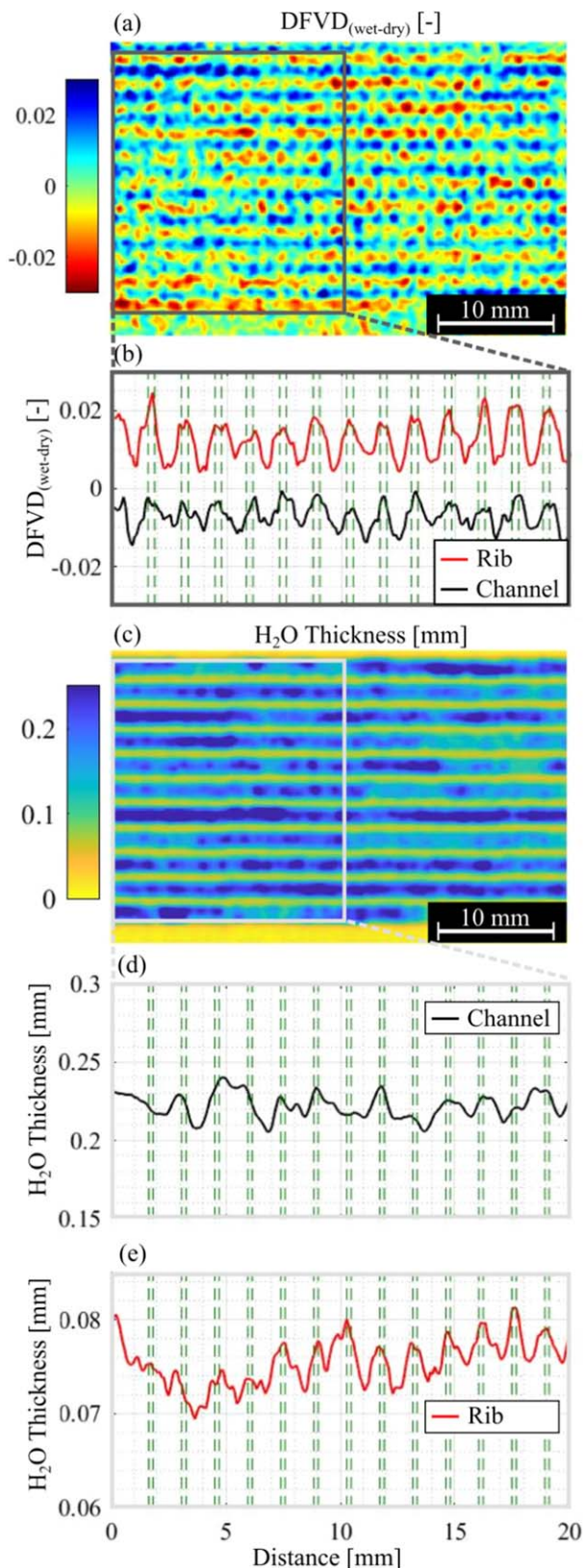
Figure 12. (a) DFVD$_{(wet-dry)}$ and (c) H$_2$O thickness image acquired with a total exposure time of 60 min during fuel cell operation at 1 Acm^{-2}. Line profiles for left part of images (highlighted with grey rectangles) of (b) DFVD$_{(wet-dry)}$ for channel (black) and rib (red) regions and of H$_2$O thickness in (d) channel and (e) rib regions. Dashed green lines indicate where hydrophilic lines are located. DFVD$_{(wet-dry)}$-image is shown with Gaussian smoothing, but line profiles were evaluated based on the unfiltered image.

In the experiment presented above (Fig. 9), the cell was only operated for 10 min and thus only little water was produced. Due to the longer operation time over which results presented in Fig. 12 are averaged, more water is present in channels and GDM compared to Fig. 9. Hence, the pattern of rib/channel and hydrophilic/phobic areas is much more pronounced in the DFVD$_{(wet-dry)}$-image (Fig. 12a). From the water thickness image (Fig. 12c), we cannot identify hydrophilic regions by eye, but the analysis of water in rib regions (Fig. 12e) reveals a similar pattern as observed for the drying procedure presented in Fig. 11. Hydrophilic regions under the ribs contain on average 5 μm more water compared to hydrophobic regions under the ribs. For channel regions (Fig. 12d), no such distinction of hydrophilic and phobic regions is possible based on the attenuation contrast image. On the contrary, the analysis of the DFVD$_{(wet-dry)}$ for channel regions reveals a clear pattern between hydrophobic and hydrophilic regions (Fig. 12b). The analysis of the water distribution in the GDM overlapping with channels is possible because large water clusters present in the channels do not contribute to DF contrast. This is true as long as DF images are reconstructed for phase-stepping images that were acquired over a sufficiently long time, because water moving in the channels can cause artefacts in DF images. Our strategy to reduce the impact of such artefacts is discussed in the next subsection.

***Reduction of water movement artefacts by golden ratio G0-stepping.*—**The reason why moving water clusters in channels cause artefacts is as follows: the DF image is reconstructed from several "phase-step" images, which are acquired for different positions of G0. If the transmission changes due to water droplets moving in the channels during the acquisition time of these phase-step images, the DF value is misevaluated. To minimize the impact of such artefacts, we applied a special G0-stepping procedure (see experimental section) inspired by the golden ratio scan strategy used in computed tomography.[86] Conventionally, G0 is stepped between monotonically increasing, equidistant positions over a distance corresponding to one G0 period. Generally in neutron grating interferometry around 9 or more phase-steps are recorded.[77] With the golden ratio scan strategy, the grating positions are not placed in a monotonically increasing order. Therefore, a change of transmission during the acquisition of a G0 scan is less likely to be mistaken as an interference modulation, as the values before and after the change of transmission are spread over the G0 period. In supplementary information (Fig. S4), it is schematically illustrated why the golden ratio phase stepping strategy is advantageous to retrieve more reliable fitting results under conditions with changing transmission over the evaluation time.

The reduction of artefacts in the DFVD$_{(wet-dry)}$-image with golden ratio G0-stepping compared to normal G0-stepping is visualized in Fig. 13. The two DFVD$_{(wet-dry)}$-image sequences displayed in Figs. 13a and 13c consist of DF images, which are each reconstructed from 27 phase-step images (4.5 min total exposure time). In the sequence acquired with normal G0-stepping (Fig. 13a) we can observe that the DFVD$_{(wet-dry)}$, for several channels in different images, is much lower than the surrounding and than in the same position in other images. These are artefacts caused by the movement of water accumulated in channels as described above. Such artefacts are clearly reduced in the image sequence acquired with golden ratio G0-stepping (Fig. 13c). The reduction of artefacts with golden ratio G0-stepping is corroborated by computing the pixel-wise standard deviation over 15 DFVD$_{(wet-dry)}$-images of the two different sequences. The standard deviation of the sequence acquired with normal G0-stepping (Fig. 13b) is higher in channel regions compared to rib regions, while this effect is much lower with golden ratio G0-stepping (Fig. 13d). The advantage of golden ratio over normal G0-stepping manifests not only in the fact that artefacts are reduced, but it also allows to choose the evaluation time for the reconstruction of a DF image *a posteriori* in a completely flexible manner. With normal
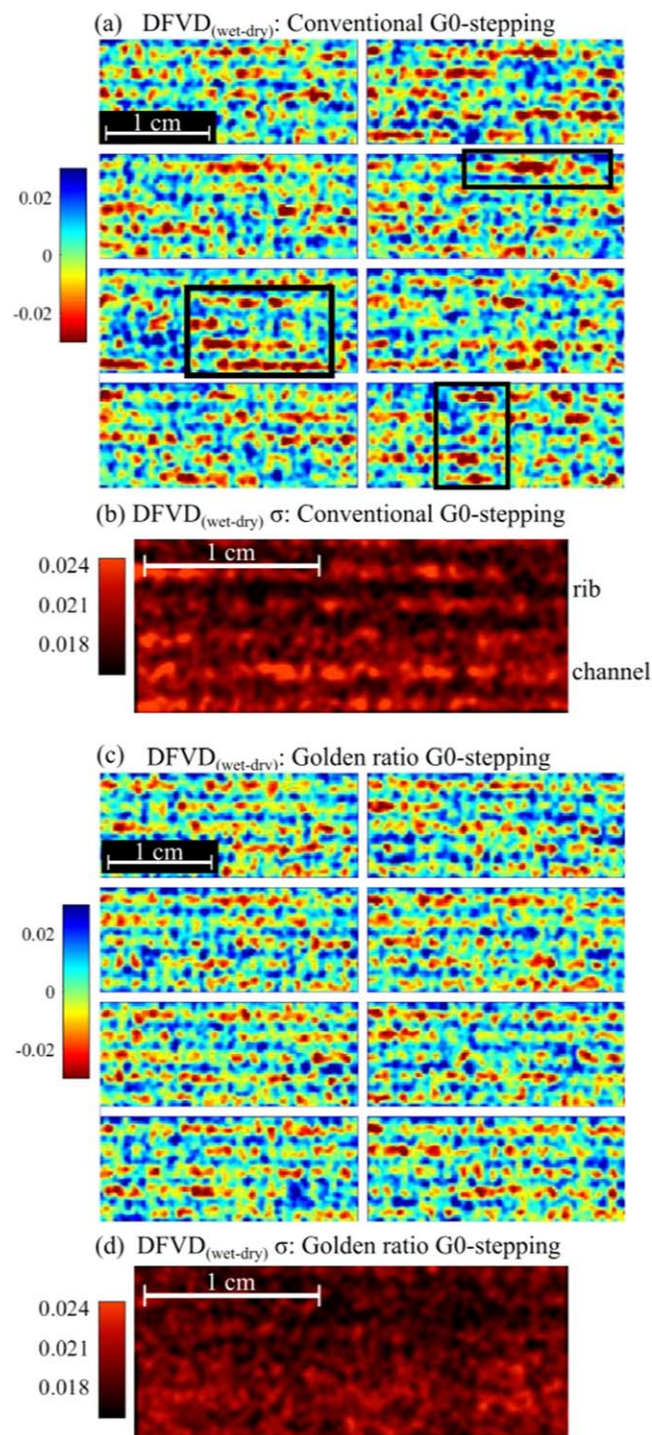
Figure 13. Impact of water moving in channels: image sequences of DFVD$_{(wet-dry)}$ (each retrieved from 27 phase-step images with a total exposure time of 4.5 min) with (a) conventional G0-stepping and (c) golden ratio G0-stepping. Black rectangles highlight regions with artefacts. (b), (d) Corresponding standard deviation (σ) images showing σ for each pixel calculated based on 15 individual DFVD$_{(wet-dry)}$-images. DFVD$_{(wet-dry)}$-images are shown with Gaussian smoothing.

G0-stepping there are constraints given by the number of phase-steps acquired per oscillation.

Conclusions

We demonstrated that neutron dark-field (DF) imaging is a promising method for the water distribution analysis in gas diffusion media (GDM) during operando fuel cell experiments. Thanks to the development of an improved nGI setup with increased visibility, we were able to significantly increase the contrast-to-noise ratio (CNR) of DF images, which allows performing measurements faster and more accurately than with previous setups. The visibility of the nGI setup reaches 57% with a monochromatic beam (3.5 ± 0.26 Å) and a neutron aperture diameter of 20 mm. A visibility of 21% is obtained with a white beam and an aperture of 40 mm. Despite the reduction of visibility with the white beam and a larger aperture an increase of the figure of merit is demonstrated this way because the visibility loss is more than compensated by the increase of neutron flux. Further, we optimized the grating parameters in such a way that we obtained a DF contrast which does not saturate when two GDM (anode and cathode side) are mounted in the fuel cell. We demonstrated, that DF imaging is a valuable method to study inhomogeneities in the dry GDM microstructure, as for example the higher compression of the GDM in the rib region results in a lower DF contrast compared to less compressed GDM areas. Operando fuel cell experiments were performed with a GDM at the cathode which was in-house modified to feature patterned wettability. With conventional attenuation contrast imaging it is—under certain conditions—possible to quantify an increase of less than 10% in water thickness in hydrophilic regions compared to hydrophobic regions. However, this analysis is only possible for rib regions, because large water clusters in the flow field channels prevent the analysis of GDM water overlapping with channels. With DF-imaging, we measure under the ribs a significant difference (increase of 100% of the measured signal) for hydrophilic compared to hydrophobic regions because the DF contrast is sensitive to the size and shape of microstructures. For channel areas, a difference between hydrophobic and hydrophilic regions was also evidenced with DF imaging when the image acquisition time for phase-step images is long enough (>15 min).

Finally, the artefacts in the DF image caused by water movement in channels in operando measurements were studied. We demonstrated that the appearance of such artefacts is considerably reduced by using a golden ratio phase-stepping scan strategy. The artefacts are reduced to a level, which allows the analysis of water distributed in the whole GDM with shorter acquisition times (e.g. 5 min) compared to normal phase stepping.

Besides the application of neutron DF imaging to study aspects influencing the water management of fuel cells or microstructural inhomogeneities of GDM, there is a wide range of possible applications for other electrochemical devices. The method enables the spatially resolved analysis of processes occurring at the microstructure level and behind materials opaque to visible light and X-rays. Therefore, it can be applied, for example, to investigate such processes in redox flow batteries, electrolyzers or lithium batteries.

ORCID

M. Siegwart https://orcid.org/0000-0002-5374-1473
V. Manzi-Orezzoli https://orcid.org/0000-0002-0998-0792
T. J. Schmidt https://orcid.org/0000-0002-1636-367X
P. Boillat https://orcid.org/0000-0002-5683-8086

References

1. P. Boillat, P. Oberholzer, A. Kaestner, R. Siegrist, E. H. Lehmann, G. G. Scherer, and A. Wokaun, *J. Electrochem. Soc.*, **159**, F210 (2012).

2. T. Rosen, J. Eller, J. Kang, N. I. Prasianakis, J. Mantzaras, and F. N. Buchi, *J. Electrochem. Soc.*, **159**, F536 (2012).
3. F. N. Büchi and P. Boillat, *Encyclopedia of Applied Electrochemistry*, ed. R. F. Savinell, K. Ota, and G. Krysa (Springer Science + Business Media LLC, New York) p. 1661 (2014).
4. J. P. Owejan, T. A. Trabold, and M. M. Mench, *Int. J. Heat. Mass Tran.*, **71**, 585 (2014).
5. J. Ihonen, M. Mikkola, and G. Lindbergh, *J. Electrochem. Soc.*, **151**, A1152 (2004).
6. H. Li et al., *J. Power Sources*, **178**, 103 (2008).
7. J. St Pierre, D. P. Wilkinson, S. Knights, and M. L. Bos, *J. New Mat. Elect. Syst.*, **3**, 99 (2000).
8. J. T. Gostick, M. W. Fowler, M. D. Pritzker, M. A. Ioannidis, and L. M. Behra, *J. Power Sources*, **162**, 228 (2006).
9. A. El-Kharouf, T. J. Mason, D. J. L. Brett, and B. G. Pollet, *J. Power Sources*, **218**, 393 (2012).
10. M. Mortazavi and K. Tajiri, *J. Fuel. Cell Sci. Tech.*, **11**, 021002 (2014).
11. I. V. Zenyuk, D. Y. Parkinson, L. G. Connolly, and A. Z. Weber, *J. Power Sources*, **328**, 364 (2016).
12. R. R. Rashapov, J. Unno, and J. T. Gostick, *J. Electrochem. Soc.*, **162**, F603 (2015).
13. A. Jayakumar, S. P. Sethu, M. Ramos, J. Robertson, and A. Al-Jumaily, *Ionics*, **21**, 1 (2015).
14. M. V. Williams, E. Begg, L. Bonville, H. R. Kunz, and J. M. Fenton, *J. Electrochem. Soc.*, **151**, A1173 (2004).
15. N. Parikh, J. S. Allen, and R. S. Yassar, *Fuel Cells*, **12**, 382 (2012).
16. G. Velayutham, J. Kaushik, N. Rajalakshmi, and K. S. Dhathathreyan, *Fuel Cells*, **7**, 314 (2007).
17. J. Biesdorf, A. Forner-Cuenca, T. J. Schmidt, and P. Boillat, *J. Electrochem. Soc.*, **162**, F1243 (2015).
18. J. Becker, C. Wieser, S. Fell, and K. Steiner, *Int. J. Heat Mass Tran.*, **54**, 1360 (2011).
19. J. Park, H. Oh, T. Ha, Y. I. Lee, and K. Min, *Appl Energ*, **155**, 866 (2015).
20. F. Lapicque, M. Belhadj, C. Bonnet, J. Pauchet, and Y. Thomas, *J. Power Sources*, **336**, 40 (2016).
21. Y. Lee, B. Kim, Y. Kim, and X. G. Li, *Appl Energ*, **88**, 5111 (2011).
22. B. T. Huang, Y. Chatillon, C. Bonnet, F. Lapicque, S. Leclerc, M. Hinaje, and S. Rael, *Fuel Cells*, **12**, 347 (2012).
23. D. K. Qiu, H. Janssen, L. F. Peng, P. Irmscher, X. M. Lai, and W. Lehnert, *Appl Energ*, **231**, 127 (2018).
24. A. Bazylak, *Int J Hydrogen Energ*, **34**, 3845 (2009).
25. A. Arvay, E. Yli-Rantala, C. H. Liu, X. H. Peng, P. Koski, L. Cindrella, P. Kauranen, P. M. Wilde, and A. M. Kannan, *J. Power Sources*, **213**, 317 (2012).
26. C. Totzke et al., *J. Power Sources*, **253**, 123 (2014).
27. J. Lee, R. Yip, P. Antonacci, N. Ge, T. Kotaka, Y. Tabuchi, and A. Bazylak, *J. Electrochem Soc*, **162**, F669 (2015).
28. J. Eller, J. Roth, F. Marone, M. Stampanoni, and F. N. Büchi, *J. Electrochem Soc*, **164**, F115 (2017).
29. P. Deevanhxay, T. Sasabe, S. Tsushima, and S. Hirai, *J. Power Sources*, **230**, 38 (2013).
30. D. Muirhead, R. Banerjee, J. Lee, M. G. George, N. Ge, H. Liu, S. Chevalier, J. Hinebaugh, K. Han, and A. Bazylak, *Int J Hydrogen Energ*, **42**, 29472 (2017).
31. F. Akitomo, T. Sasabe, T. Yoshida, H. Naito, K. Kawamura, and S. Hirai, *J. Power Sources*, **431**, 205 (2019).
32. R. T. White, S. H. Eberhardt, Y. Singh, T. Haddow, M. Dutta, F. P. Orfino, and E. Kjeang, *Sci Rep-Uk*, **9**, 1843 (2019).
33. A. K. C. Wong, N. Ge, P. Shrestha, H. Liu, K. Fahy, and A. Bazylak, *Appl Energ*, **240**, 549 (2019).
34. A. Schneider, C. Wieser, J. Roth, and L. Helfen, *J. Power Sources*, **195**, 6349 (2010).
35. J. Eller and F. N. Buchi, *J. Synchrotron Radiat.*, **21**, 82 (2014).
36. D. Spernjak, A. K. Prasad, and S. G. Advani, *J. Power Sources*, **170**, 334 (2007).
37. A. Bazylak, D. Sinton, Z. S. Liu, and N. Djilali, *J. Power Sources*, **163**, 784 (2007).
38. M. Mortazavi, A. D. Santamaria, J. Z. Benner, and V. Chauhan, *J Electrochem Soc*, **166**, F3143 (2019).
39. R. Alink, D. Gerteisen, and W. Merida, *Fuel Cells*, **11**, 481 (2011).
40. Y. Aoyama, K. Suzuki, Y. Tabe, T. Chikahisa, and T. Tanuma, *J Electrochem Soc*, **163**, F359 (2016).
41. K. W. Feindel, S. H. Bergens, and R. E. Wasylishen, *J. Power Sources*, **173**, 86 (2007).
42. T. Kotaka, S. Tsushima, and S. Hirai, *ECS Trans.*, **11**, 445 (2007).
43. J. Zhang, D. Kramer, R. Shimoi, Y. Ono, E. Lehmann, A. Wokaun, K. Shinohara, and G. G. Scherer, *Electrochim. Acta*, **51**, 2715 (2006).
44. A. Forner-Cuenca, J. Biesdorf, A. Lamibrac, V. Manzi-Orezzoli, F. N. Büchi, L. Gubler, T. J. Schmidt, and P. Boillat, *J Electrochem Soc*, **163**, F1038 (2016).
45. J. I. S. Cho et al., *Energy*, **170**, 14 (2019).
46. D. Kramer, J. Zhang, R. Shimoi, E. Lehmann, A. Wokaun, K. Shinohara, and G. G. Scherer, *Electrochim. Acta*, **50**, 2603 (2005).
47. Y. Wu, J. I. S. Cho, T. P. Neville, Q. Meyer, R. Ziesche, P. Boillat, M. Cochet, P. R. Shearing, and D. J. L. Brett, *J. Power Sources*, **399**, 254 (2018).
48. A. D. Santamaria, M. K. Becton, N. J. Cooper, A. Z. Weber, and J. W. Park, *J. Power Sources*, **293**, 162 (2015).
49. Y. Wu et al., *J. Power Sources*, **412**, 597 (2019).
50. J. P. Owejan, T. A. Trabold, J. Gagliardo, D. L. Jacobson, R. N. Carter, D. S. Hussey, and M. Arif, *J. Power Sources*, **171**, 626 (2007).
51. M. A. Hickner, N. P. Siegel, K. S. Chen, D. S. Hussey, and D. L. Jacobson, *J. Electrochem. Soc.*, **157**, B32 (2010).
52. P. Oberholzer and P. Boillat, *J. Electrochem. Soc.*, **161**, F139 (2014).
53. S. Gößling, M. Klages, J. Haußmann, P. Beckhaus, M. Messerschmidt, T. Arlt, N. Kardjilov, I. Manke, J. Scholta, and A. Heinzel, *J. Power Sources*, **306**, 658 (2016).
54. P. Boillat, E. H. Lehmann, P. Trtik, and M. Cochet, *Current Opinion in Electrochemistry*, **5**, 3 (2017).
55. J. P. Owejan, J. J. Gagliardo, S. R. Falta, and T. A. Trabold, *J. Electrochem. Soc.*, **156**, B1475 (2009).
56. P. Boillat, A. Iranzo, and J. Biesdorf, *J. Electrochem. Soc.*, **162**, F531 (2015).
57. J. P. Owejan, T. A. Trabold, D. L. Jacobson, M. Arif, and S. G. Kandlikar, *Int J Hydrogen Energ*, **32**, 4489 (2007).
58. P. Oberholzer, P. Boillat, R. Siegrist, A. Kastner, E. H. Lehmann, G. G. Scherer, and A. Wokaun, *Electrochem. Commun.*, **20**, 67 (2012).
59. Q. Meyer et al., *Electrochim. Acta*, **211**, 478 (2016).
60. M. Siegwart, R. P. Harti, V. Manzi-Orezzoli, J. Valsecchi, M. Strobl, C. Grunzweig, T. J. Schmidt, and P. Boillat, *J. Electrochem. Soc.*, **166**, F149 (2019).
61. C. Grunzweig, F. Pfeiffer, O. Bunk, T. Donath, G. Kuhne, G. Frei, M. Dierolf, and C. David, *Rev. Sci. Instrum.*, **79**, 053703 (2008).
62. F. Pfeiffer, M. Bech, O. Bunk, P. Kraft, E. F. Eikenberry, C. Brönnimann, C. Grünzweig, and C. David, *Nat. Mater.*, **7**, 134 (2008).
63. M. Strobl, C. Grüenzweig, A. Hilger, I. Manke, N. Kardjilov, C. David, and F. Pfeiffer, *Phys. Rev. Lett.*, **101**, 123902 (2008).
64. T. H. Jensen et al., *Phys. Rev. B*, **82**, 214103 (2010).
65. V. Revol, B. Plank, R. Kaufmann, J. Kastner, C. Kottler, and A. Neels, *Ndt & E. Int*, **58**, 64 (2013).
66. B. Betz, R. Harti, M. Strobl, J. Hovind, A. Kaestner, E. Lehmann, H. Van Swygenhoven, and C. Grünzweig, *Rev. Sci. Instrum.*, **86**, 123704 (2015).
67. R. P. Harti, M. Strobl, B. Betz, K. Jefimovs, M. Kagias, and C. Grünzweig, *Sci Rep-Uk*, **7**, 44588 (2017).
68. M. Kagias, Z. T. Wang, K. Jefimovs, and M. Stampanoni, *Appl. Phys. Lett.*, **110**, 014105 (2017).
69. R. P. Harti, J. Valsecchi, P. Trtik, D. Mannes, C. Carminati, M. Strobl, J. Plomp, C. P. Duif, and C. Grunzweig, *Sci Rep-Uk*, **8**, 17845 (2018).
70. T. Reimann, S. Muhlbauer, M. Horisberger, B. Betz, P. Böni, and M. Schulz, *J. Appl. Crystallogr.*, **49**, 1488 (2016).
71. Y. Kim, J. Kim, D. Kim, D. S. Hussey, and S. W. Lee, *Review of scientific instruments*, **90**, 033701 (2019).
72. M. Strobl, *Sci Rep-Uk*, **4**, 7243 (2014).
73. K. Creath, *Progress in Optics*, ed. E. Wolf (Elsevier, Amsterdam)349 (1988).
74. T. Weitkamp, A. Diaz, B. Nohammer, F. Pfeiffer, T. Rohbeck, P. Cloetens, M. Stampanoni, and C. David, *Developments in X-ray Tomography Iv*, **5535**, 137 (2004).
75. R. Andersson, L. F. van Heijkamp, I. M. de Schepper, and W. G. Bouwman, *J. Appl. Crystallogr.*, **41**, 868 (2008).
76. T. Krouglov, I. M. de Schepper, W. G. Bouwman, and M. T. Rekveldt, *J. Appl. Crystallogr.*, **36**, 117 (2003).
77. R. P. Harti, M. Strobl, M. Morgano, J. Valsecchi, and C. Grunzweig, *Rev. Sci. Instrum.*, **88**, 103704 (2017).
78. J. Kim, K. H. Lee, C. H. Lim, T. Kim, C. W. Ahn, G. Cho, and S. W. Lee, *Rev. Sci. Instrum.*, **84**, 063705 (2013).
79. R. P. Harti, C. Kottler, J. Valsecchi, K. Jefimovs, M. Kagias, M. Strobl, and C. Grunzweig, *Opt. Express*, **25**, 1019 (2017).
80. T. Donath et al., *J. Appl. Phys.*, **106**, 054703 (2009).
81. Y. Kim, J. Kim, D. Kim, D. S. Hussey, and S. W. Lee, *Rev. Sci. Instrum.*, **89**, 033701 (2018).
82. Y. Kim, J. Valsecchi, J. Kim, S. W. Lee, and M. Strobl, *Rev. Sci. Instrum.*, **9**, 18973 (2019).
83. A. Forner-Cuenca, J. Biesdorf, A. Lamibrac, V. Manzi-Orezzoli, F. N. Buchi, L. Gubler, T. J. Schmidt, and P. Boillat, *J. Electrochem. Soc.*, **163**, F1038 (2016).
84. V. Manzi-Orezzoli, M. Siegwart, M. Cochet, T. J. Schmidt, and P. Boillat, *J. Electrochem. Soc.*, **167**, 054503 (2020).
85. A. P. Kaestner, S. Hartmann, G. Kühne, G. Frei, C. Grünzweig, L. Josic, F. Schmid, and E. H. Lehmann, *Nucl Instrum Meth A*, **659**, 387 (2011).
86. A. Kaestner, B. Munch, P. Trtik, and L. Butler, *Opt. Eng.*, **50**, 123201 (2011).
87. nGImagic/TaPy: TaPy 0.2, (2019), https://github.com/nGImagic/TaPy.
88. S. Marathe, L. Assoufid, X. H. Xiao, K. Ham, W. W. Johnson, and L. G. Butler, *Rev. Sci. Instrum.*, **85**, 013704 (2014).
89. M. Siegwart, R. Woracek, J. I. Márquez Damián, A. S. Tremsin, V. Manzi-Orezzoli, M. Strobl, T. J. Schmidt, and P. Boillat, *Rev. Sci. Instrum.*, **90**, 103705 (2019).
90. Y. Seki, T. Shinohara, J. D. Parker, W. Ueno, T. Samoto, W. Yashiro, A. Momose, Y. Otake, and Y. Kiyanagi, *EPL (Europhysics Letters)*, **123**, 12002 (2018).
91. A. Gustschin, T. Neuwirth, A. Backs, M. Schulz, and F. Pfeiffer, *Rev. Sci. Instrum.*, **89**, 103702 (2018).
92. T. Samoto, H. Takano, and A. Momose, *Jpn. J. Appl. Phys.*, **58**, SDDF12 (2019).